Journal of Power Sources 202 (2012) 291–298

Contents lists available at SciVerse ScienceDirect

Journal of Power Sources

journal homepage: www.elsevier.com/locate/jpowsour

SnO_2–MnO_2 composite powders and their electrochemical properties

A.M. Hashem[a], H.M. Abuzeid[a], A.E. Abdel-Ghany[a], A. Mauger[b], K. Zaghib[c,*], C.M. Julien[d]

[a] National Research Centre, Inorganic Chemistry Department, Behoes St., Dokki, Cairo, Egypt
[b] Université Pierre et Marie Curie – Paris6, Institut de Minéralogie et Physique de la Matière Condensée (IMPMC), 4 place Jussieu, 75005 Paris, France
[c] Institut de Recherche d'Hydro-Québec (IREQ), 1800 Bd Lionel-Boulet, Varennes, Québec, Canada J3X 1S1
[d] Université Pierre et Marie Curie – Paris6, Physicochimie des Electrolytes, Colloïdes et Sciences Analytiques (PECSA), UMR 7195, 4 place Jussieu, 75005 Paris, France

ARTICLE INFO

Article history:
Received 11 October 2011
Received in revised form
17 November 2011
Accepted 17 November 2011
Available online 26 November 2011

Keywords:
Manganese dioxide
Tin oxide deposit
Cathode
Lithium batteries

ABSTRACT

Nanosized cryptomelane manganese dioxide (MDO) and its SnO_2-coated product were prepared through a redox reaction between $KMnO_4$ and Mn(II) acetate. XRD analysis showed the cryptomelane-type structure for both materials. Chemical analysis detected the presence of K in parent and K and Sn in coated oxide. The coating was evidenced by TEM images, which display a thin layer of SnO_2 at the surface of nanosized MnO_2 particles. Vibrational spectroscopic measurements confirmed the integrity of the MnO_2 lattice. The net effect of the SnO_2 coating results in better electrochemical performance of the Li//MnO_2 cells.

1. Introduction

Transition-metal oxides are an important class of materials for a variety of electrochemical applications including batteries, supercapacitors, electrocatalysts and sensors [1]. Among them, manganese dioxide (MDO) is an interesting compound due to its advantages including easy preparation and low cost. It is environmentally friendly, it has excellent electrochemical properties and it is a safe material [2,3]. MnO_2 has an important structural flexibility and appears in a number of crystallographic polymorphs, such as α-, β-, γ-, δ-, and ε-MnO_2, where the main structural motif is made of MnO_6 octahedra sharing edges and corners in different connectivity schemes [4]. Among these MDOs, α-MnO_2 has received special attention as a cathode material for rechargeable lithium batteries, since the large 2×2 tunnels, which exist in the crystalline lattice of α-MnO_2, are believed to facilitate the accommodation and motion of the inserting Li^+ ions [5]. It is well known that the kinetics of the intercalation process of Li^+ ions is determinant to the electrochemical performance of the MnO_2 electrode. Therefore, how to accelerate the diffusion of Li^+ ions becomes an important problem to be solved [6].

Nanoscale materials exhibit peculiar and fascinating properties superior to their bulk counterparts. Electrode active materials with small crystalline particle sizes usually show higher electrochemical activities, good discharge performances and better rate capability than the large-sized particles, due to their high specific surface areas and smaller diffusion length for the Li^+ intercalation [7]. Furthermore, several techniques have been developed for the preparation of nanostructured MDOs with significant progress [8]. Nanosized MDOs for electrode materials are typically fabricated via electrochemical or chemical routes. Recently, MnO_2 nanowires [9,10] and nanorods [11,12] have been reported. Li and co-workers [13,14] have reported the hydrothermal preparation of α-MnO_2 nanowires by oxidizing $MnSO_4$ in either $KMnO_4$ or $(NH_4)_2S_2O_8$.

However, the killing drawback of MDOs used as electrode materials in electrochemical systems like batteries or supercapacitors is the poor cyclic property. A slow capacity fade upon repeated charge/discharge cycling has been observed in many cells using Mn-oxide as cathode materials [15,16]. The origin of this capacity loss has been attributed to the dissolution into the electrolyte through the following reaction $2Mn^{3+} \rightarrow Mn^{4+} + Mn^{2+}$, which occurs in the presence of trace of acids. The disproportionation process occurs on the electrode at the end of the discharge, accompanied by a structural transition due to Jahn–Teller distortion. A very simple strategy to overcome this disadvantage consists in surface modification with a protective coating, which acts as a stabilizer of the MDO framework. The use of another oxide could be envisaged such as Al_2O_3, ZnO, ZrO_2 or SiO_2, which have been successfully used to protect $LiMn_2O_4$ spinel particles [17–20]. Long et al. have shown that ultrathin polymer coatings onto nanostructured MnO_2 birnessite-type renders the electrodes stable in acid electrolytes [21]. Recently, Jan et al. [22] have

* Corresponding author. Tel.: +1 450 652 8019; fax: +1 450 652 8424.
E-mail address: zaghib.karim@ireq.fr (K. Zaghib).

0378-7753/$ – see front matter © 2011 Elsevier B.V. All rights reserved.
doi:10.1016/j.jpowsour.2011.11.053

demonstrated the compatibility of MnO_2 with SnO_2 to make supercapacitors.

In the present work, we would like to address the important question of the Mn dissolution in organic electrolyte and how to reduce it by surface protection. We have synthesized nanosized α-MnO_2 and SnO_2-coated particles by the wet-chemical method developed in previous works [23,24], which was successful in preparing Sn- and Co-doped α-MnO_2 hollandite-type with high thermal stability. The structural and magnetic properties of materials were investigated by X-ray diffraction (XRD), transmission electronic microscopy (TEM), Fourier transform infrared (FTIR) and Raman scattering (RS) spectroscopy and SQUID experiments. We evidence the efficiency of the tin oxide film at the surface of α-MnO_2 particles; the electrochemical tests show improvement of the performance for MnO_2. The capacity fading is reduced by 30% after deposition of a 10-nm thick SnO_2 film at the surface of the MnO_2 nanoparticles.

2. Experimental

2.1. Synthesis

The α-MnO_2 nanosized particles were synthesized by oxidation of manganese acetate by potassium permanganate in an aqueous solution. The mixture of $Mn(II)(CH_3COO)_2$ and $KMnO_4$ (from Aldrich) with molar ratio 2:3 was stirred for 3 h in 100 mL distilled water at 60 °C. A black precipitate was formed. The precipitate was separated by filtration and dried at 100 °C for 12 h. The final product (named P-MnO_2 hereafter) was obtained by heat treatment at 450 °C for 5 h in an ambient atmosphere.

The SnO_2-coated samples were prepared like P-MnO_2 using $SnCl_2$ as a coating agent. 1 g of MnO_2 was mixed with 0.1 g of $SnCl_2$ in 50 mL absolute ethanol by stirring the solution during 3 h at room temperature. Further stirring at 80 °C was continued to evaporate ethanol. After complete vaporization of ethanol, the dried sample was calcined at 400 °C for 1 h in an ambient atmosphere to obtain Sn coated MnO_2 (named SnO_2/MnO_2 hereafter).

2.2. Apparatus

XRD patterns were recorded using a Philips X'Pert apparatus equipped with a CuKα X-ray source (λ = 1.54056 Å). Data were collected in the 2θ range 10–80°. Raman spectra were collected with a double monochromator (Jobin-Yvon model U1000) using the 514.5 nm line from the Spectra-Physics 2020 Ar-ion laser. The spectra were recorded using a backscattering geometry, and the laser power was kept below 25 mW to prevent the degradation of materials by the laser during data acquisition. All spectroscopic data were collected with a spectral resolution of 2 cm^{-1}. FTIR spectra were recorded using a Bruker model IFS113v interferometer equipped with a MCT mid-IR and DTGS/PE detectors. Specimens were prepared by the disk method using powders mixed with CsI (1:300) and pressing them at 5 tons cm^{-2} with good transparency for IR radiation. TGA measurements were carried out using a thermal gravimetric analyzer (Perkin Elmer, TGA 7 series) in the temperature range of 30–1000 °C in air at a heating rate of 10 °C min^{-1}. Inductive coupled plasma spectrometry (ICP, Shimadzu ICPS-1000IV) was used to determine K and Sn contents in the prepared samples. The sample was dissolved in HCl acid then diluted to 250 mL by distilled water. ICP measurements were carried out in standard measuring flask. JEOL, Transmission Electron Microscope (TEM, JEM-1230) Japan was used to investigate the prepared samples. The magnetic measurements (susceptibility and magnetization) were performed with two fully automated SQUID magnetometers (Quantum Design MPMSXL) in the temperature range 4–300 K. Powders were placed into small plastic vial, placed in a holder and finally inserted into the helium cryostat of the SQUID apparatus.

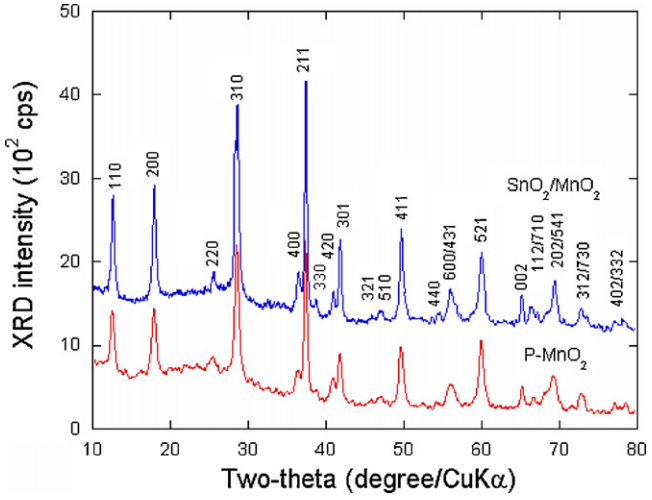

Fig. 1. X-ray powder diffraction patterns of P-MnO_2 and SnO_2/MnO_2 synthesized by the oxidation method of Mn acetate by $KMnO_4$ at 60 °C. The precursor was fired at 450 °C for 12 h in air.

2.3. Electrochemical tests

The electrochemical tests of Li//MnO_2 cells were carried out at room temperature. The positive electrodes were a mixture of 80 wt.% active material, 10 wt.% of carbon black and 5 wt.% of polytetrafluoroethylene as binder. The Li//MnO_2 cells were housed in a Teflon laboratory – cell hardware employing Li-metal foil as counter electrode. The electrolyte was 1.0 mol L^{-1} $LiPF_6$ in a mixture of ethylene carbonate (EC) and diethyl carbonate (DEC) (1:1, v/v). A microporous polypropylene film (Celgard 2500) was used as a separator. The lithium uptake of discharge was estimated using the current passed and the mass of the electrode material. Measurements were performed 2 C-rate discharge current in a potential range 1.5–3.5 V vs. Li^0/Li^+ using a Mac-pile battery cycler.

3. Results and discussion

3.1. Structure and morphology

Fig. 1 shows the XRD pattern for pristine α-MnO_2 sample prepared by the redox reaction between $KMnO_4$ and manganese acetate with post-synthesis heat treatment at 450 °C and together with the XRD diagram of SnO_2-coated α-MnO_2 sample. The diffractograms show similar features with Bragg peaks characteristics of the cryptomelane-like MnO_2 phase. The coating did not modify the XRD spectrum. These spectra are indexed using the tetragonal phase with *I*4/*m* space group according to the JCPDS 44-0141 standard file [25]. The predominant (3 1 0) and (1 2 1) Bragg lines corresponds to the *d*-spacing 3.11 and 2.40 Å, respectively. No extra peaks related to impurities or SnO_2 was observed. The XRD pattern clearly indicates the highly crystalline nature of the α-MnO_2 and SnO_2/MnO_2 samples. Refinements of the XRD data by a least square method using the tetragonal system lead to the lattice parameters $a = 9.861(1)$ Å, $c = 2.859(2)$ Å and $V = 278.3(7)$ $Å^3$, for P-MnO_2 and $a = 9.854(9)$ Å, $c = 2.857(3)$ Å and $V = 277.1(5)$ $Å^3$ for the SnO_2/MnO_2. These values show that no significant modification of the structure occurred during the coating process. So, we consider that the bulk of the cryptomelane phase remains the same.

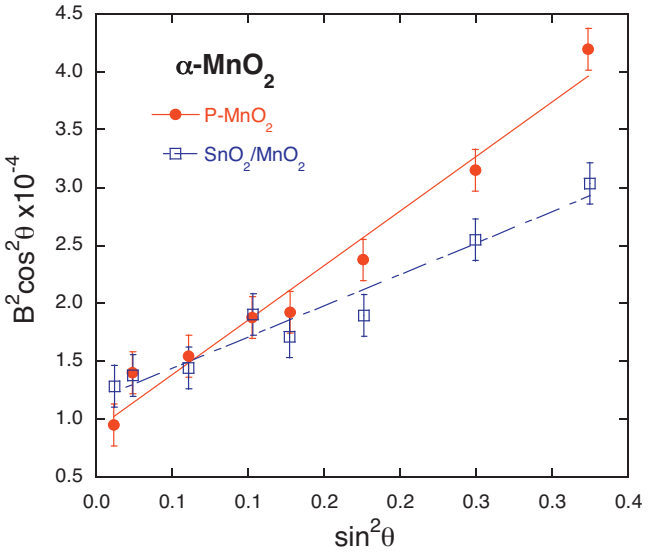

Fig. 2. Analysis of the full-width B at half-maximum of the XRD peaks according to Eq. (1). B is in radian.

In general, several factors can contribute to the broadening of peaks in X-ray diffraction [25,26]. In the case of manganese compounds, we have already shown that two factors need being taken into account: the size of the crystallites and the strain field [27]. We then follow this previous work and combine the Scherrer's equation for crystallite size and the Bragg's law for diffraction to determine crystallite size L and micro-strain local $\langle e^2 \rangle$ by using the following equation

$$B^2 \cos^2\theta = 16\langle e^2 \rangle \sin^2\theta + \frac{K^2\lambda^2}{L^2} \quad (1)$$

where B is the full-width at half-maximum (fwhm) in radian, after correction of the instrumental broadening for finely powdered silicon powder, θ is the diffraction angle and K is a near-unity constant related to crystallite shape. The plot of the first member as a function of $\sin^2\theta$ is reported in Fig. 2 for the pristine MnO_2 and its SnO_2-coated product. The plots are well fit by straight lines, in agreement with Eq. (1). The slope of the linear fit of the data provides us with the value of the strain $\langle e^2 \rangle$, while the extrapolation to $\sin\theta = 0$ provides us with the value of the coherence length L. Note that the linear law shown in the figure gives indirect evidence that L is independent of q. The crystallites are then spherical as first approximation, so that we take for the constant K the value appropriate to this particular case, $K = 0.9$.

We find that L is not significantly affected by the coating, as $L = 14.6$ and 12.8 nm for α-MnO_2 and SnO_2/MnO_2, respectively,

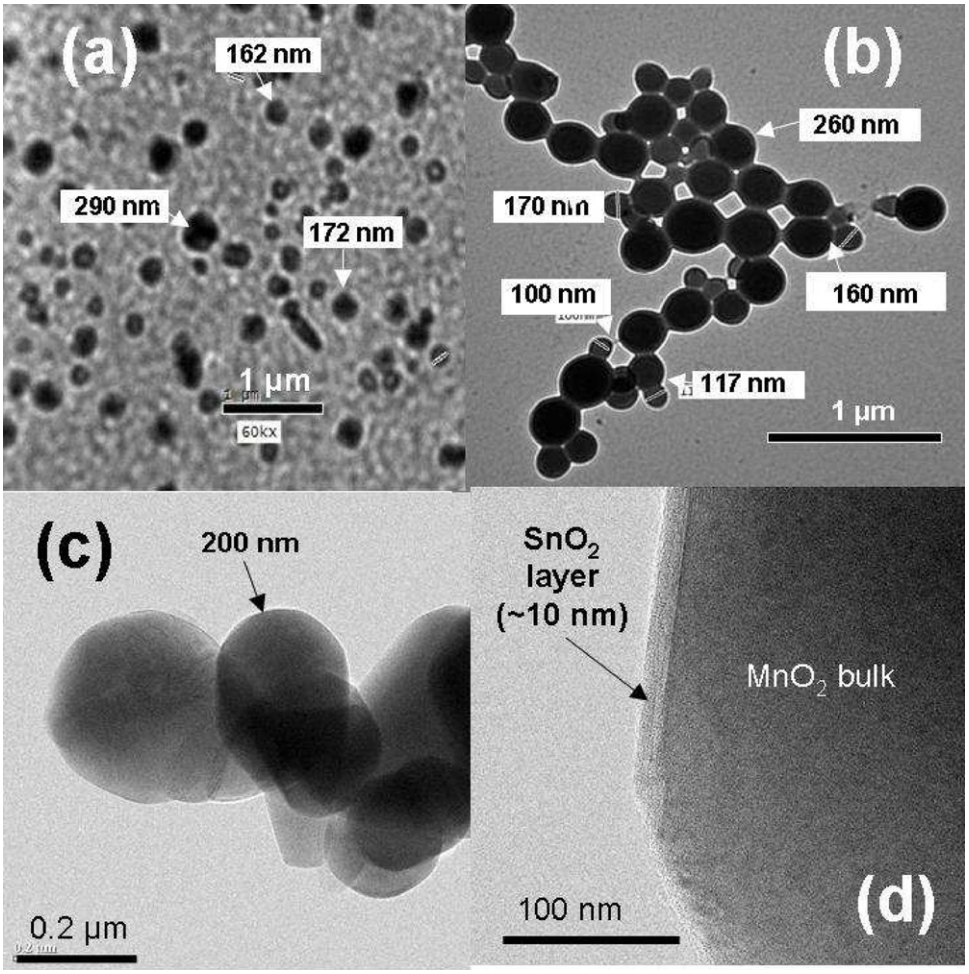

Fig. 3. TEM micrographs of P-MnO_2 (a) and SnO_2-coated MnO_2 (b) powders synthesized by the oxidation method of Mn acetate by $KMnO_4$ at 60 °C. The precursor was fired at 450 °C for 12 h in air. HRTEM images (c and d) taken at higher magnification shows the spherical particle of the pristine materials and SnO_2-coated with a thin layer 10 nm thick, respectively.

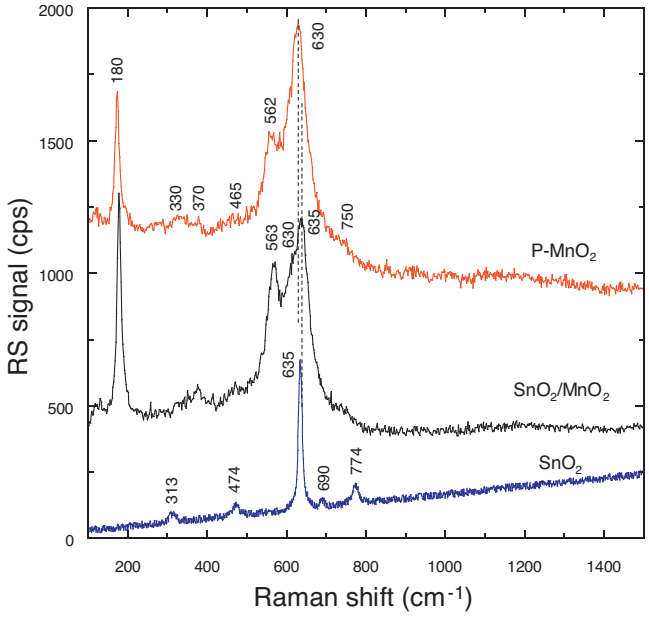

Fig. 4. Raman scattering spectra of P-MnO_2 and SnO_2/MnO_2 samples. Powders were synthesized by the oxidation method of Mn acetate by $KMnO_4$ at 60 °C. The precursor was fired at 450 °C for 12 h in air.

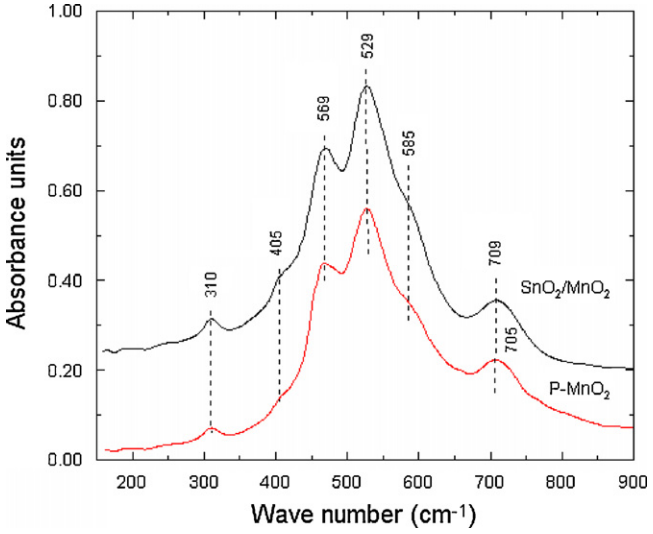

Fig. 5. FTIR absorption spectra of pristine MnO_2 and SnO_2-coated MnO_2 samples. Powders were synthesized by the oxidation method of Mn acetate by $KMnO_4$ at 60 °C. The precursor was fired at 450 °C for 12 h in air.

according to Fig. 2, which can be merged in $L = 13.7 \pm 0.9$ nm. On another hand $\langle e^2 \rangle$ is significantly affected by the SnO_2 deposit. The crystallite strains are 7.5×10^{-3} and 5.8×10^{-3} ($\pm 0.18 \times 10^{-3}$) for α-MnO_2 and SnO_2/MnO_2, respectively. The larger strain is attributable to a small oxygen deficiency often met in the MDO lattice, which results in a small fraction of Mn^{3+} ions. Due to the different ionic radius of Mn^{3+} plus the fact that it is a Jahn–Teller ion, the valence change from Mn^{4+} to Mn^{3+} for a small fraction of cations in α-MnO_2 generates local distortions of the lattice evidenced by the increase strain field. In MnO_2, the presence of Mn^{3+} originates from K^+ ions, and from oxygen vacancies. The elemental analysis (ICP results) shows that the amount of K is almost the same for both the P-MnO_2 and the SnO_2/MnO_2 samples, namely 5.5 mol.%. The reduction of the strain field in the SnO_2/MnO_2 sample is thus solely attributable to the decrease of the concentration of oxygen vacancy, since each oxygen vacancy is accompanied by the oxidation of two Mn^{4+} in Mn^{3+}. Therefore, the smaller strain field gives the first evidence that the SnO_2 coating has reduced the amount of oxygen vacancies. Further evidenced will be provided by magnetic properties.

The TEM micrographs of α-MnO_2 and SnO_2/MnO_2 are presented in Fig. 3a and b with 60k× magnification. These patterns show that the samples have almost spherical morphology. Both α-MnO_2 and SnO_2/MnO_2 samples are nano-sized particle with dimension in the range 150–270 nm. The particle size distribution is narrow and centered at 200 nm. Note this is larger than the coherent length L that corresponds to the mean crystallite size, so that each particle is composed of an assembly of crystallites separated by grain boundaries. Fig. 3c and d shows the HRTEM images of α-MnO_2 and SnO_2/MnO_2 samples, respectively, for which particles have spherical-like shape. A remarkable thin layer of SnO_2 ca. 10 nm is encapsulating the MnO_2 particles (Fig. 3d). These figures depict that the shape of cryptomelane particles remains nearly the same upon SnO_2 coating.

3.2. Optical spectroscopy

Fig. 4 shows the RS spectrum of P-MnO_2 (curve a) and SnO_2/MnO_2 (curve b) recorded in the spectral range 150–1500 cm^{-1}. The Raman bands at 180, 330, 370, 465, 562, 630 and 750 cm^{-1} are those of the cryptomelane α-MnO_2 phase in good agreement with values of the literature [28,29]. The SnO_2 coating does not bring any change in the local structure of α-MnO_2, almost the same RS bands are observed after coating process, except for the appearance of a new band at ca. 635 cm^{-1} that is the dominant A_{1g} Raman-active mode of SnO_2 (curve c) [30]. Let us emphasize that both α-MnO_2 and SnO_2–MnO_2 oxides have two diagnostic RS bands in the high-frequency region, at 562 and 630 cm^{-1}. They belong to the A_g spectroscopic species that originate from the stretching vibrations of MnO_6 octahedra within the tetragonal framework. Here, no structural change in the local structure was observed in the Raman spectrum after coating by SnO_2. This is the proof that the tin atoms do not insert inside the large tunnel of the α-MnO_2. Because of the high absorption for MnO_2 for laser light in the visible range ($\lambda = 514.5$ nm), the depth penetration is $\delta \approx 40$–50 nm. That is why Raman spectroscopy allows us to probe together the coating layer ($\delta \approx 10$ nm) plus the surface of the particles.

Fig. 5 shows the FTIR spectra of P-MnO_2 and SnO_2/MnO_2 samples. Absorption spectra display the characteristic features of the cryptomelane framework with Mn–O stretching modes in the high-wavenumber range and Mn–O bending modes in the low-wavenumber region [29]. Eight infrared-active modes are predicted by factor group analysis for the α-MnO_2 material ($3B_u + 5E_u$). The FTIR spectrum (Fig. 5) displays six bands, which appear in the range 300–750 cm^{-1}. The stretching mode of MnO_6 octahedra along the double-chain is located at 705 cm^{-1}. In the far-IR region, the band at 310 cm^{-1} is diagnostic of minerals of the cryptomelane-like structure. It is also interesting to remark that the FTIR features involve mainly the vibrations of the octahedral MnO_6 skeleton and do not include a significant contribution from the large cations in the channel. The shape of the absorption spectrum of the SnO_2-coated material is identical to that of the starting material, but a slight shift (ca. 4 cm^{-1}) is observed in the position of the stretching mode (709 cm^{-1}), which confirms the change in the average oxidation state of Mn ions. This frequency shift toward the high-wavenumber side corresponds to an increase of the content of Mn^{4+} ions, which is consistent with the reduction in the Mn^{3+} concentration linked to the decrease of oxygen vacancies evidenced by the structural properties, in good agreement with the magnetic data shown below.

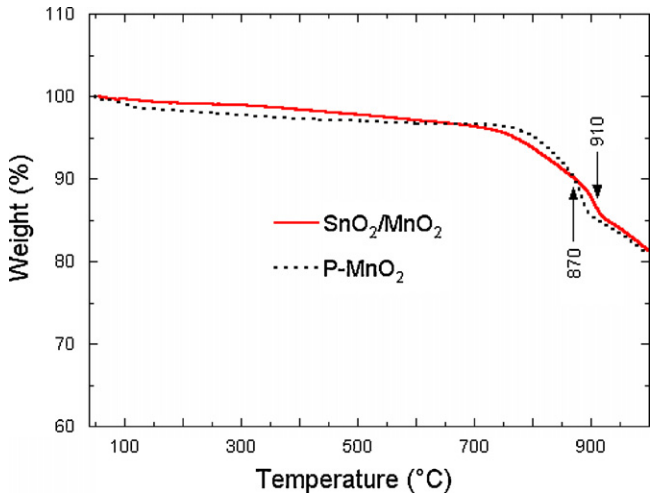

Fig. 6. Thermogravimetric analysis of P-MnO_2 and SnO_2/MnO_2 samples. Measurements were carried out in air in the range 25–900 °C at the heating rate 10 °C min^{-1}.

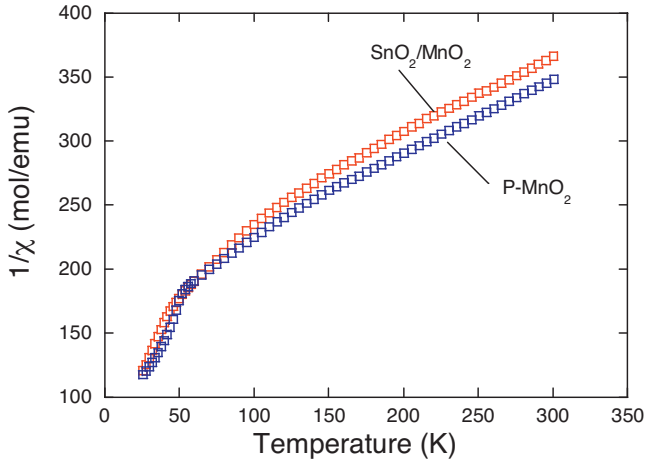

Fig. 7. Temperature dependence of the reciprocal magnetic susceptibility $\chi^{-1}(T)$ of P-MnO_2 and SnO_2/MnO_2 powers. Measurements were carried out with an applied magnetic field 10 kOe.

3.3. Thermal analysis

Fig. 6 shows the thermogravimetric analysis of α-MnO_2 and SnO_2/MnO_2 oxides recorded in normal atmosphere. Structural stability for both samples was observed from these curves. Both MDOs start to convert to Mn_2O_3 above 750 °C, while the transformation to Mn_3O_4 is expected above 1000 °C. The remarkable increase in thermal stability observed for these oxides may be related to the presence of a high content of potassium cations inside 2 × 2 tunnels. It is well known that K^+ ions play an important role as a stabilizing cation [23,24]. It has been reported that the thermal decomposition reaction of MnO_2 containing low K^+ content occurs in two steps according to the phenomena given in Refs. [31,32]. The structural change from MnO_2 to Mn_2O_3 was observed at 540 °C by Muraoka et al. [32], whereas the second decomposition from Mn_2O_3 to Mn_3O_4 occurs in the range 900–1000 °C. Our results reported in Fig. 6 are consistent with these prior works. The decomposition to Mn_2O_3 starts above 700 °C. Up to this temperature, the difference between the two curves in Fig. 6 is so small that it could simply be due to a surface effect, and the weight loss does not exceed 5%. This result is not surprising since both samples have the same K^+ concentration. However, the inflection point that can points to the more important decomposition due to the loss of oxygen is switched from 870 to 910 K for the SnO_2-coated sample.

3.4. Magnetic properties

Magnetic experiments are powerful tools to study the fundamental properties and to analyze the purity of samples containing transition-metal elements [33–35]. Fig. 7 shows the temperature dependence of the inverse magnetic susceptibility $\chi^{-1}(T)$ measured in field H = 10 kOe, for α-MnO_2 and SnO_2/MnO_2 samples. The magnetization curves $M(H)$ reported for both samples are shown in Fig. 8a and b. At temperature $T \geq 50$ K, the system is paramagnetic, while $\chi^{-1}(T)$ deviates from linearity, especially below 100 K, so that the Curie–Weiss law is not satisfied. The strong downward curvature between 50 and 100 K reveals an increasing component of an impurity. As a consequence, we expect that the magnetic susceptibility curve in the paramagnetic regime is the sum of two Curie–Weiss contribution: the first being the fingerprint of the MnO_2 phase, the second coming from the impurity. The magnetic susceptibility χ_m is then

$$\chi = (1-y)\frac{C_p}{T-\theta_p} + y\frac{C_i}{T-\theta_i}, \quad (2)$$

where the index p refers to the α-MnO_2 contribution, while the index i refers to the impurity; y is the fraction of Mn atoms involved in the impurity. The result of the fit of the experimental curves by Eq. (2) is suited to describe the paramagnetic behavior in the whole range T > 60 K. For both coated and non-coated samples, the impurity part is found to be the same, namely y = 0.03, θ_i = 50 K. This value of θ_i is characteristic of a manganese compound that orders in a magnetic state with the onset of a remanent magnetization at this temperature of 50 K: this is the signature of Mn_3O_4. The presence of this impurity is not surprising, since the Mn_3O_4 is the dominant impurity in many Mn-compounds [36,37], including β-MnO_2 [38]. In most cases, however, the amount of Mn_3O_4 can be determined by the amplitude of the jump of magnetization associated to the onset of the ferrimagnetic ordering of Mn_3O_4.

Like in the prior works [36,38], we find here that this impurity can be detected only by magnetic measurements. Note the Curie–Weiss contribution of Mn_3O_4 at temperatures T > 100 K is given by a Curie Weiss law with a paramagnetic Curie temperature that is different from 50 K, since the asymptotic value of θ_i deduced from measurements at very high temperature is −564 K [39]. Above 100 K, however, the contribution of the Mn_3O_4 to χ is negligible anyway, because of the small value of y.

All the parameters linked to the impurity (C_i, y, θ_I) are found to be the same in the P-MnO_2 and the SnO_2/MnO_2 samples. Therefore, the coating has no impact on the Mn_3O_4 that is neutral in the coating process. Only the intrinsic contribution of MnO_2 has changed. The effective magnetic moment μ_{eff} carried by Mn in the intrinsic part is given by the relation

$$\mu_{eff} = 2.84 C_p^{1/2} \mu_B, \quad (3)$$

where μ_B is the Bohr magnetron, and C_p is expressed in mole unit. The result of the fit (Fig. 7) is μ_{eff} = 3.71 μ_B for α-MnO_2 and 3.75 μ_B for SnO_2/MnO_2. For the coated sample, the result is lower than $\mu_{eff}(Mn^{4+})$ = 3.87 μ_B expected for Mn^{4+}, taking into account the quenching of the orbital momentum by the crystal field. The lower value for μ_{eff} is due to the presence of potassium cations in the 2 × 2 tunnels that leads the chemical formula $K_yMn_{8-y}{}^{4+}Mn_y{}^{3+}O_{16-z}$ with $0.2 \leq x \leq 1.0$ for the cryptomelane framework [40], plus oxygen vacancies in concentration z, so that the Mn^{3+} concentration is $x = y + 2z$. The deficit of magnetic moment is attributable to this residual concentration of Mn^{3+} ($3d^4$ configuration) in the low-spin

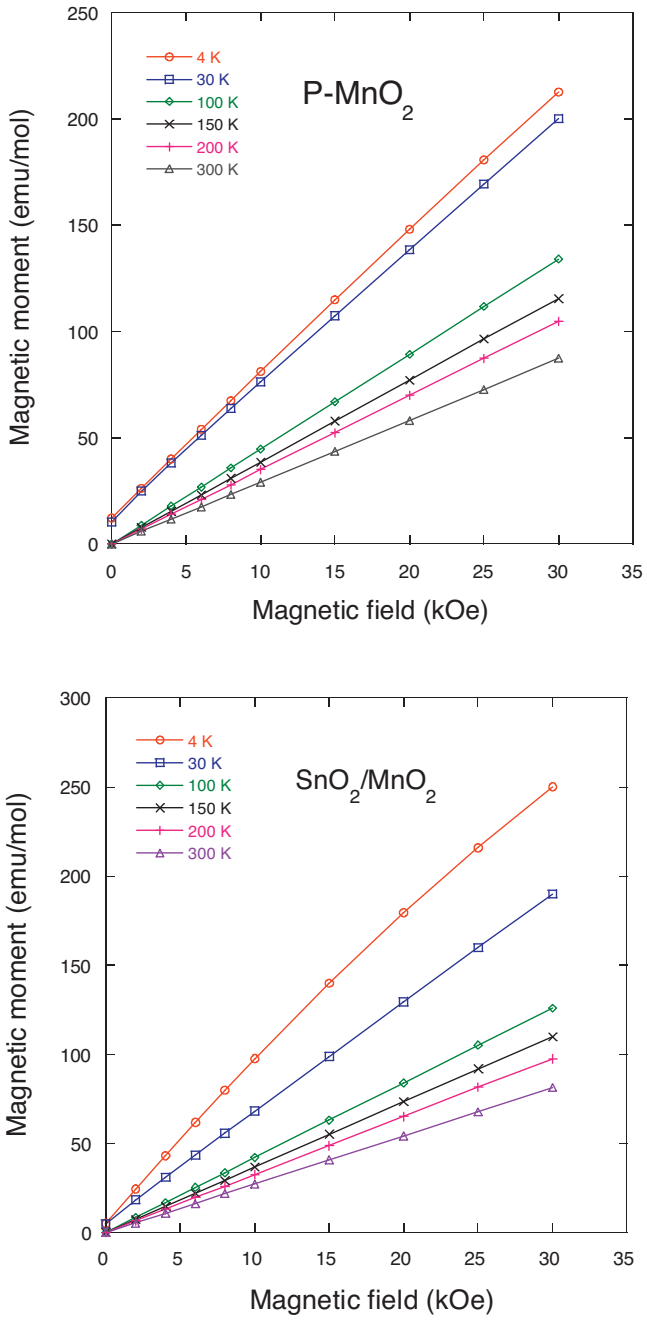

Fig. 8. Isothermal plots of the magnetic moment as a function of the applied magnetic field for (a) P-MnO_2 and (b) SnO_2/MnO_2 sample. Note the non linearity of the graphs at temperature below 100 K.

state with the spin $S = 0$. The fraction x of manganese in the trivalent state can be determined from the relation

$$\mu_{eff}{}^2 = x \times 0 + (1 - x) \times 3.87^2. \quad (4)$$

The result is $x = 8.2\%$ in P-MnO_2. This concentration is decreased to 6.2% in SnO_2/MnO_2. Taking into account that $y = 5.5$ at.%, the concentration of oxygen vacancies is $z = 1.3$ at.% in the P-MnO_2 sample, reduced to $z = 0.3$ at.% in the SnO_2/MnO_2 sample. We can thus conclude that the SnO_2 coating has avoided the loss of oxygen in MnO_2. This result is consistent with the result of the analysis of the XRD spectra in Section 3.1 and the analysis of the optical spectra in Section 3.2. Note, however, that magnetic experiments are the tool that allowed us to quantify this concentration of oxygen vacancies. The results of the redox titration obtained by the method described by the Suib's group [41] are in good agreement with these results from magnetic experiments.

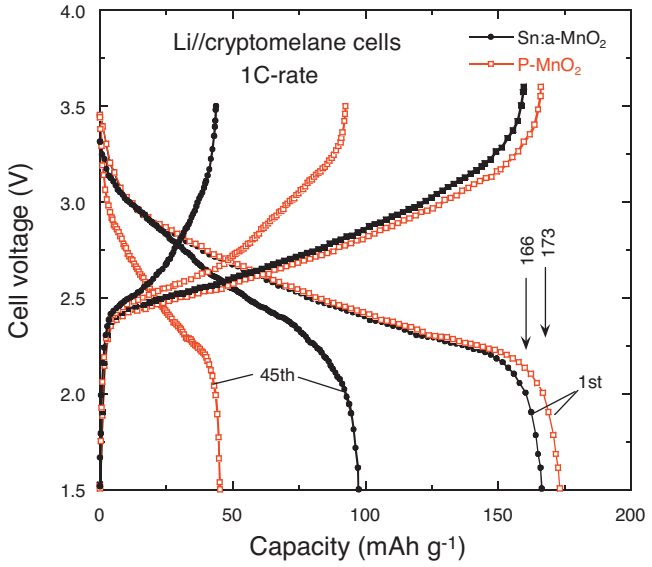

Fig. 9. Discharge–charge curves for Li cells with P-MnO_2 and SnO_2/MnO_2 electrode materials. The electrolyte was 1.0 mol L^{-1} $LiPF_6$ in a mixture of ethylene carbonate (EC) and diethyl carbonate (DEC) (1:1, v/v). Data were collected at 1 C rate in potential range 1.5–3.5 V vs. Li^0/Li^+.

3.5. Electrochemical properties

Fig. 9 shows the discharge curves for Li cells with α-MnO_2 and SnO_2-coated MnO_2 electrode material using 1.0 mol.L^{-1} $LiPF_6$ in EC-DEC as electrolyte at the 1st and 45th cycle. Measurements were carried out within potential range 1.5–3.5 V vs. Li^0/Li^+ at the 1 C rate. For both electrode materials the discharge curves are characterized by a slightly sloping profile with an average cell potential at ca. 2.65 V. An initial discharge capacity of 173 and 166 mAh g^{-1} was obtained for P-MnO_2 and SnO_2/MnO_2, respectively. It means that about 0.56 and 0.54 Li^+ ions were inserted per MnO_2 formula unit, respectively. SnO_2/MnO_2 shows also similar polarization in comparison with P-MnO_2. SnO_2-coated MnO_2 sample that retained about 58% from its initial capacity after 45th cycle, whereas P-MnO_2 retained only 27% in the same discharge condition. The better electrochemical performance upon the 45th cycle is attributed to the surface modification of MnO_2. Thus, we assume that the thin SnO_2 layer preserves the MnO_2 particle without noticeable modification of the electronic transport of the MnO_2 part. Apart the very small decrease of the initial discharge capacity, the "SnO_2-film" acts as a protective layer around MnO_2 particles that prevents dissolution of Mn-ions into the organic electrolyte. This postulation agrees very well with results reported before for Sn-treated MoO_3 [42]. Moreover, these results can be compared with the results reported recently for vanadium substituted cryptomelane MnO_2 oxides [6], for which 117 mAh g^{-1} was delivered at 0.38 mA cm^{-2} current density.

Fig. 10a and b shows the incremental capacity, i.e. the derivative dQ/dV vs. potential, and the cyclic voltammograms for Li cells with P-MnO_2 and SnO_2/MnO_2 electrode material, respectively. The voltammograms exhibit one set de redox peaks observed for both oxides at ca. 2.32 and 2.51 V vs. Li^0/Li^+ at a scan rate 0.1 mV s^{-1} (Fig. 10b), which are the redox features of Li insertion/extraction into/from the cryptomelane MnO_2 framework. These results are consistent with the derivative dQ/dV spectrum, according to which the reduction appears at 2.29 V (Fig. 10a). About the same value of potential has been found after coating the sample by SnO_2. Fig. 11

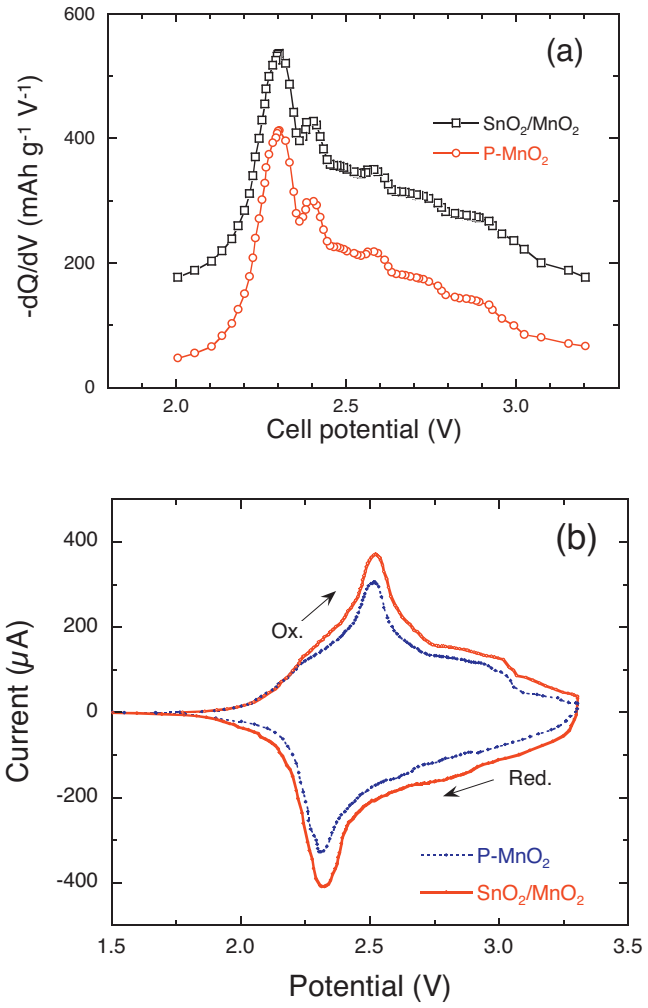

Fig. 10. (a) Incremental capacity, dQ/dV vs. potential, and (b) cyclic voltammogram recorded at 0.1 mV s^{-1} scanning rate for P-MnO_2 and SnO_2/MnO_2 electrode materials.

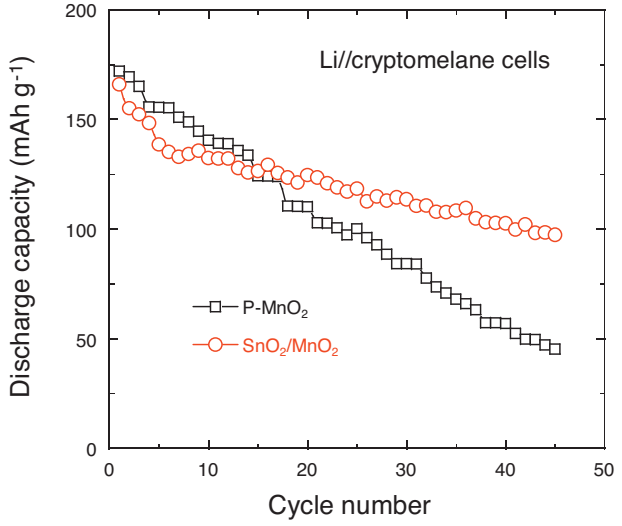

Fig. 11. Discharge capacity vs. cycle number for Li cells with P-MnO_2 and SnO_2/MnO_2 electrode materials. Tests were carried out at 1 C rate in the potential range 1.5–3.5 V vs. Li^0/Li^+.

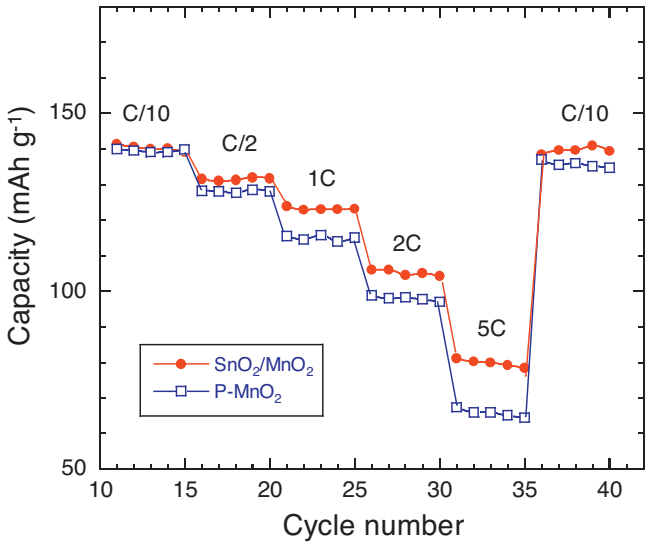

Fig. 12. Discharge capacity between 3.5 and 1.5 V vs. Li^+/Li^0 at various C-rate as a function of cycle number for the P-MnO_2 and SnO_2/MnO_2 electrode materials.

represents the discharge capacity as a function of cycle number for the two types of positive electrode in lithium cells. It may be noted that the discharge capacity in the first 15 cycles is higher for pristine α-MnO_2 than for SnO_2-coated electrode. This reinforces the view that the process is related to the structural stability of the coated particles which could be due to the absence of Mn^{3+} dissolution in the electrolyte. It is also attributed to the conservation of the kinetics of the Li^+ ions insertion process into the MnO_2 host because the 10 nm thick SnO_2 coating layer is porous enough for easy Li^+ ions migration. Then, for next cycles, the capacity fade for α-MnO_2 is somewhat greater (2% per cycle) compared with 0.75% for SnO_2/MnO_2. Obviously, the MnO_2 electrode material coated 10-nm thick SnO_2 film appears better at long-term cycling. The decline in charge capacity in P-MnO_2 could be attributed to delamination and partial dissolution of manganese dioxide films into the electrolytes [43]. If this explanation is retained, our results show that the SnO_2 coat has been efficient to protect the P-MnO_2 from interacting with the electrolyte. It is also speculated that other factors may also be involved, such as changes in the electronic conductivity during cycling associated with changes in oxidation states [44]. If this explanation is retained, the improvement we have observed in the present work is attributable to the decrease of oxygen vacancies resulting in the better integrity of the material.

For rate performance comparison, the discharge capacity at various C-rate as a function of cycle number for the P-MnO_2 and the surface modified SnO_2/MnO_2 cathode material is presented in Fig. 12. For each sample, the cells were tested five times at each C-rate. From these experiments, it is shown that the capacity is recovered with a better efficiency (99.5%) for the surface modified sample than for the P-MnO_2 cathode material (98.7%) after 25 cycles. The stability of the surface modified SnO_2/MnO_2 sample is evidenced by the recovery of the initial capacity.

4. Conclusion

In this work we studied the effect of the SnO_2-coating on the MnO_2 particles. Pristine MnO_2 was prepared by wet chemistry method through redox reaction between Mn(II) acetate and $KMnO_4$. SnO_2 coating onto MnO_2 particles was carried out in an ambient atmosphere. The cryptomelane framework was characterized by structural, magnetic and vibrational spectroscopic experiments. No significant structure change was observed after

SnO_2 coating as observed from XRD, TGA, FTIR and RS characterizations. 200 nm sized particles were observed for both parent and SnO_2-coated oxides from TEM images. The particles contained a small amount (5.5 at.% after ICP measurements) of K^+ ions intercalated in the 2×2 channels. The magnetic measurements show that the cryptomelane framework contains a concentration 1.3 at.% of oxygen vacancies, while this concentration almost vanishes after coating. A remarkable improvement in electrochemical performance of SnO_2-coated oxide in terms of discharge capacity and low capacity fading upon 45 cycles as compared with pristine MnO_2. This improvement is the translation on the electrochemical properties of the reduction in oxygen vacancies that improves the integrity of the particles, and protects the MnO_2 particle form interacting with the electrolyte.

References

[1] G.M. Whitesides, J.P. Mathias, C.T. Seto, Science 254 (1991) 1312.
[2] Q. Luo, Q. Muraliganth, A. Manthiram, Solid State Ionics 180 (2009) 703.
[3] L.J. Fu, H. Liu, C. Li, Y.P. Wu, E. Rahm, R. Holze, H.Q. Wu, Prog. Mater. Sci. 50 (2005) 881.
[4] T. Gao, H. Fjellvag, P. Norby, Anal. Chim. Acta 648 (2009) 235.
[5] N. Kijima, Y. Sakata, Y. Takahashi, J. Akimoto, T. Kumagai, T. Igarashi, T. Shimizu, Solid State Ionics 180 (2009) 616.
[6] M.K. Gulbinska, S.L. Suib, J. Power Sources 196 (2011) 2149.
[7] Z.P. Feng, G.R. Li, J.H. Zhong, Z.L. Wang, Y.N. Ou, Y.X. Tong, Electrochem. Commun. 11 (2009) 706.
[8] K. Katakura, S. Nishimura, Z. Ogumi, J. Power Sources 146 (2005) 217.
[9] J.H. Kim, T. Ayalasomayajula, V. Gona, D. Choi, J. Power Sources 183 (2008) 366.
[10] A. Débart, J.A. Paterson, J.L. Bao, P.G. Bruce, Angew. Chem. Int. Ed. 47 (2008) 4521.
[11] Y.Y. Yang, L.F. Xiao, Y.Q. Zhao, F.Y. Wang, Int. J. Electrochem. Sci. 3 (2008) 67.
[12] H.N. Yoo, D.H. Park, S.J. Hwang, J. Power Sources 185 (2008) 1374.
[13] X. Wang, Y.D. Li, Chem. Commun. 7 (2002) 764.
[14] X. Wang, Y.D. Li, J. Am. Chem. Soc. 124 (2002) 2880.
[15] R.J. Gummow, A. de Kock, M.M. Thackeray, Solid State Ionics 69 (1994) 59.
[16] D.H. Jang, Y.J. Shin, S.M. Oh, J. Electrochem. Soc. 143 (1996) 2204.
[17] S.W. Lee, K.S. Kim, H.S. Moon, H.J. Kim, B.W. Cho, W.I. Cho, J.B. Ju, J.W. Park, J. Power Sources 126 (2004) 150.
[18] J. Tu, X.B. Zhao, J. Xie, G.S. Cao, D.G. Zhuang, T.J. Zhu, J.P. Tu, J. Alloys Compd. 432 (2007) 313.
[19] S. Lim, J. Cho, Electrochem. Commun. 10 (2008) 1478.
[20] D. Arumugam, K.G. Paruthimal, J. Electroanal. Chem. 624 (2008) 197.
[21] Nano Lett. 3 (2003) 1155.
[22] J. Yan, E. Khoo, A. Sumboja, P.S. Lee, ACS Nano 4 (2010) 4247.
[23] A.M. Hashem, H.A. Mohamed, A. Bahloul, A.E. Eid, C.M. Julien, Ionics 14 (2008) 7.
[24] A.M. Hashem, H.M. Abu-Zeid, K. Nikolowski, H. Ehrenberg, J. Alloys Compd. 497 (2010) 300.
[25] H.P. Klug, L.E. Alexander, X-ray Diffraction Procedures for Polycrystalline and Amorphous Materials, Wiley, New York, 1974.
[26] C. Hammond, The Basic of Crystallography and Diffraction, Oxford University Press, New York, 1997.
[27] N. Amdouni, F. Gendron, A. Mauger, H. Zarrouk, H.C.M. Julien, Mater. Sci. Eng. B 129 (2006) 64–75.
[28] T. Gao, M. Glerup, F. Krumeich, R. Nesper, H. Fjellvag, P. Norby, J. Phys. Chem. C 112 (2008) 13134.
[29] C.M. Julien, M. Massot, C. Poinsignon, Spectrochim. Acta A 60 (2004) 689.
[30] S.H. Sun, G.W. Meng, G.X. Zhang, T. Gao, B.Y. Geng, L.D. Zhang, J. Zuo, Chem. Phys. Lett. 376 (2003) 103.
[31] T. Ohzuku, I. Tari, T. Hirai, Electrochim. Acta 27 (1982) 1049.
[32] Y. Muraoka, H. Chiba, T. Atou, M. Kikuchi, K. Hiraga, Y. Syono, S. Sugiyama, S. Yamamoto, J.C. Grenier, J. Solid State Chem. 144 (1999) 136.
[33] A. Ait Salah, K. Zaghib, A. Mauger, F. Gendron, C.M. Julien, Phys. Status Solidi (a) 203 (2006) 1.
[34] J.B. Goodenough, Magnetism and the Chemical Bond, Wiley, New York, 1963.
[35] C.M. Julien, A. Ait-Salah, A. Mauger, F. Gendron, Ionics 12 (2006) 21.
[36] M. Kopec, J.R. Dygas, F. Krok, A. Mauger, F. Gendron, C.M. Julien, J. Phys. Chem. Solids 69 (2008) 955.
[37] K. Dwight, N. Menyuk, Phys. Rev. 119 (1960) 1470.
[38] A. Bahloul, B. Nessark, F. Habelhames, C.M. Julien, Ionics 17 (2011) 239.
[39] B. Boucher, R. Buhl, M. Perrin, J. Phys. Chem. Solids 32 (1971) 2429.
[40] B. Mukherjee, Mineral. Mag. 32 (1959) 166.
[41] G.G. Xia, W. Tong, E.N. Tolentino, N.G. Duan, S.L. Brock, J.Y. Wang, S.L. Suib, Chem. Mater. 13 (2001) 1585.
[42] A.M. Hashem, G.H. Wrodnigg, M.H. Askar, M. Winter, J.H. Albering, J.O. Besenhard, Ionics 8 (2002) 183.
[43] S.C. Pang, M.A. Anderson, T.W. Chapman, J. Electrochem. Soc. 147 (2000) 444.
[44] S.F. Chin, S.C. Pang, M.A. Anderson, J. Electrochem. Soc. 149 (2002) A379.